Supporting Information for "Real-Time Structural Dynamics of the Ultrafast Solvation Process around Photo-Excited Aqueous Halides"

Supplementary Information Part A

Setup for femtosecond time-resolved electronic absorption spectroscopy

Femtosecond transient absorption measurements were performed in pure water using a home-built gravity-driven wire-guided liquid sample film device which provided a sample film of 100 μm thickness. This experimental setup has been described in detail previously [1–4]. Briefly, the system was based on a regeneratively amplified Ti:Sa laser system (Clark MXR CPA 2001) that delivers 120 fs (FWHM) pulses with 1 kHz repetition rate at a center wavelength of $\lambda = 775$ nm. The pump pulses at $\lambda_{pump} = 240$ nm with typical energies of 0.5 μJ for 1-photon excitation were generated by frequency-doubling of pulses at 480 nm delivered from a home-built non-collinear optical parametric amplifier (NOPA). Second harmonic generation (SHG) of the fundamental was used to generate the pump pulses for 2-photon excitation at $\lambda_{pump} = 387$ nm with energies of 20 μJ. Pulses provided by supercontinuum generation in CaF_2 were split to obtain broadband probe and reference pulses. The polarization of the pump pulses relative to the probe pulses was set to the magic angle using a variable Berek waveplate. The probe beam was sent through the liquid sample film, while the reference beam was sent through a horizontally adjacent spot outside the film. Detection was achieved by a CCD spectrometer equipped with two full frame transfer (FFT) back-thinned CCD cameras.

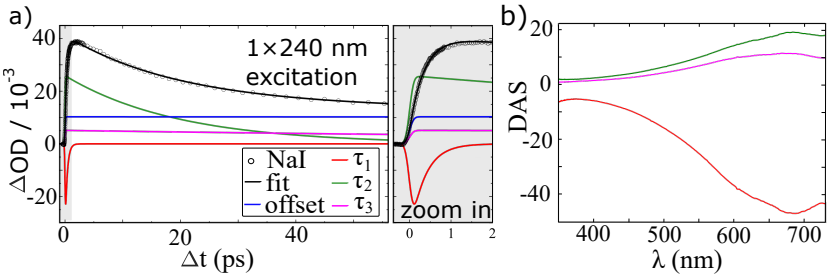

Figure 1: a) Fit to the aqueous NaI data at $\lambda = 676$ nm after 1-photon excitation. The grey area zooms into the first 2 picoseconds. Parameters of the fit are listed in Table 1. b) Decay-associated spectra from a global analysis.

In the analysis of the transient absorption signals, the change in absorption ΔA as a function of time delays Δt is modeled by first-order kinetic processes [5] as a sum of i exponentials with time constants τ_i and amplitudes a_i: $\Delta A(\Delta t) = \sum_i a_i \cdot \exp(-\Delta t/\tau_i)$.

The kinetic model is convoluted with an instrument response function (IRF) of 0.12 ps FWHM, which accounts for the broadening of the kinetics due to the pump and probe pulse width.

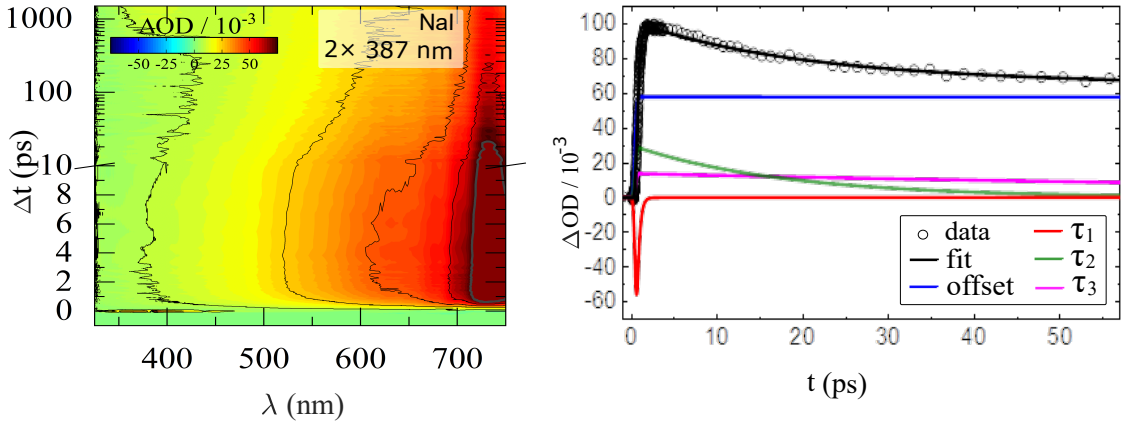

Figure 2: Optical transient absorption of NaI after 2-photon excitation and global fit with 4 parameters.

Table 1: Characteristic time constants τ_1, τ_2, τ_3 determined by fitting the transient absorption spectra. The last column shows the ratio of the amplitude a_2 (corresponding to the decay τ_2) compared to the total signal amplitude a_{total}

25 mM NaI	τ_1 (ps)	τ_2 (ps)	τ_3 (ns)	a_2/a_{total}
1×240 nm excitation	0.4(1)	18.7(3)	0.12(2)	0.6
2×387 nm excitation	0.3(2)	17.7(21)	0.12(4)	0.3

TR-XSS sample preparation and delivery

Aqueous iodide and bromide were prepared on-site from NaI and NaBr (Sigma-Aldrich, Suprapur) in MilliQ water. We studied concentrations of 20 mM and 100 mM for each sample. The aqueous solutions were delivered at SACLA by a 50 μm round jet with a flow rate of 1.5 $\frac{\text{ml}}{\text{min}}$. AT the ESRF, a 300 μm flat jet was used.

MD simulations

Simulations of solvated I^- and I^0

The MD simulations were performed with the OpenMM simulation package [6], with 5200 water molecules and one I^-/I^0 placed at the centre of the box using the LEaP program in the Amber22 package [7]. In the case of simulating I^- solvation in water, a counter Na^+ ion was placed in the

box to maintain the charge neutrality of the simulation box. The I^- and Na^+ ions are separated using a flat bottom potential with a distance of 20 Å. The water force field model used in the calculations was TIP4P^{EW}. The MD simulations are done in two steps: (1) The NPT ensemble (with a Monte Carlo Barostat set to 1 bar and 300 K temperature) is equilibrated for 10 ns. (b) Then the production runs for 10 ns using a NVT ensemble using the Langevin thermostat [8] with a friction coefficient of 1/ps to maintain a temperature of 300 K.

For the calculation of the simulated difference scattering ΔS radial distribution functions $g(r)$ are used, where $\rho(r)$ is the local density of the system at a distance r, ρ_0 is the average density of a system with N particles and V is the volume of the simulation box [9]:

$$g_{l,m}(r) = \frac{\rho(r)}{\rho_0} = \frac{V}{N}\left[\lim_{dr\to 0}\frac{N(r)}{4\pi r^2 dr}\right] \tag{1}$$

Dhabal-like weighting [10] of g(r) is applied with $r < 1$ Å set to 0 and $r > 25$ Å to eliminate effects from truncating the integral in Equation 2 in the main text. All parameters are listed in Table 2. Scattering contributions from the solute and solvation shell, henceforth called ΔS_{u+c}, are calculated with the radial distribution between iodide and oxygen (I-O) as well as iodide and hydrogen (I-H). Contributions calculated from $g(r)$ of O-O, O-H and H-H are termed ΔS_v.

	N (water)	V (Å^3)	time(ns)	production	sigma (Å)	epsilon (kcal/mol)
I^{-1}	5200	$53.97 \cdot 53.70 \cdot 54.16$	10	NVT	5.02	0.803
I^0	5200	$53.97 \cdot 53.70 \cdot 54.16$	10	NVT	5.02	0.803
I^0_{opt}	5200	$53.97 \cdot 53.70 \cdot 54.16$	10	NVT	3.75	2.51
Br^{-1}	5200	$53.97 \cdot 53.70 \cdot 54.16$	10	NVT	4.518	0.659
Br^0	5200	$53.97 \cdot 53.70 \cdot 54.16$	10	NVT	4.518	0.659

Table 2: Parameters for RDF sampling. R_{max} was 25 Å for all samples.

The Debye-formulation can be expressed in terms of radial distribution functions, as in Equation 2 in the main text:

$$S(Q) = \sum_l N_l f_l^2 + \sum_{l,m} f_l f_m \frac{N_l(N_m - \delta_{lm})}{V} 4\pi \times \int_0^\infty r^2 g_{lm}(r)\frac{\sin(Qr)}{Qr}dr, \tag{2}$$

where N_l denotes the number of atoms of type l, f indicates atomic form factors (with the dependence on Q suppressed for clarity of presentation), r is the distance between atoms, V is the irradiated volume, and δ_{lm} is the Kronecker delta. For RDFs obtained from MD simulations, the integral must be truncated at a distance R of maximum half the size of the (square) simulation cell. This truncation leads to the modification:

$$S(Q) = \sum_l N_l f_l^2 + \sum_{l,m} f_l f_m \frac{N_l(N_m - \delta_{lm})}{V_{\text{cell}}} 4\pi \times \int_0^R r^2 (g_{lm}(r) - g_0)\frac{\sin(Qr)}{Qr}dr, \tag{3}$$

where V_{cell} is the volume of the simulation cell, and where $g_0 = 0$ if both atoms of type l and m belongs to the solute (such that the RDF goes to 0 when the value of r increases) and 1 otherwise. See the literature[9, 11] for further details.

Simulations of solvated I_2^- and I_3^-

I_2^- was solvated in simulation cells of the same size as the I^- and I^0 runs, using packmol [12]. The I-I distance in I_2 was set to 3.43 Å, and the LJ parameters to 0.337 kcal/mol and 3.61 Å [13, 14]. The charge of -1 was distributed evenly over both atoms. For I_3^-, a third I atom was added to the I_2^- system using tleap from the ambertools package [7]. The charges as well as the geometry, which was kept fixed during the sampling of the solvation shell using 5000 kcal/mol Hookean restraints, were taken from Kim *et al.* [13]. Both systems were equilibrated for 2 ns in the NVT ensemble, before performing 20 ns production runs from which the RDFs were sampled every 1 ps.

Simulations of the solvent density response

For the calculation of the density response $\Delta S_{\Delta\rho}$ (see Section B), an initial 4095-molecule water box was made at 0.998 g/ml using Packmol [12] and equilibrated in the NVT ensemble at 300 K using a Langevin thermostat with a friction coefficient of 1/ps for 1 ns in OpenMM [6], followed by a 9 ns production run using the same thermostat. Then, the box size was reduced by 0.2 Å in each dimension, corresponding to a density increase of 0.0121 g/ml, and re-equilibrated for 1 ns before running a 9 ns production run with the same thermostat. The particle coordinates were saved every 1 ps. The RDFs were then sampled from both production runs using VMD [15] with a δr of 0.01 Å. The RDFs were corrected for finite-size effects using the Ganguly & van der Vegt correction [11, 16] and a Lorch-like 25 Å damping window was applied when calculating the X-ray scattering signal from the RDFs [9, 17].

Iodide MM Potential Energy Curves

For the Molecular Mechanics (MM) model used, the nonbonded interactions are given by the Coulomb and Lennard Jones (LJ) potential between atoms i and j with charges q_i, q_j

$$\begin{aligned} V_{\mathrm{ij}}(r_{\mathrm{ij}}) =& V_{\mathrm{coul}}(r_{ij}) + V_{\mathrm{LJ}}(r_{ij}) \\ =& \frac{1}{4\pi\epsilon_0}\frac{q_i q_j}{r_{ij}} + 4\epsilon_{ij}\left[\left(\frac{\sigma_{ij}}{r_{ij}}\right)^{12} - \left(\frac{\sigma_{ij}}{r_{ij}}\right)^{6}\right], \end{aligned} \tag{4}$$

where ϵ_0 is the vacuum permittivity, and r_{ij} is the distance between the particles. The LJ parameters ϵ_{ij} and σ_{ij} define the depth of the potential, and at which r_{ij} it turns from attractive to repulsive, respectively. The LJ parameters are given for individual atoms, and are combined via the Lorenz-Berthelot combination rules [18, 19] $\sigma_{ij} = (\sigma_i + \sigma_j)/2$ and $\epsilon_{ij} = \sqrt{\epsilon_i \epsilon_j}$, which are used as standard in OpenMM [6].

To find the dimer geometry that is representative of the average water orientation towards I^- in solution, we first analysed our MD trajectories to find the most expressed I-O-H angle for the 6 water molecules closest to the I atom (see Figure 3). The figure shows that the most common I-O-H angle for the closest hydrogen is $\sim 12°$. We thus create the the dimer $[\mathrm{I}\cdots\ \mathrm{H_2O}]$ with the same angle before investigating a series of I-H_2O distances r for $V(R = r_{\mathrm{IO}}) = V_{\mathrm{IO}} + V_{\mathrm{IH_1}} + V_{\mathrm{IH_2}}$. Then, for I^- and for two sets of I^0 LJ parameters shown in table 3, we calculate the potential energies for each of the spanned distances.

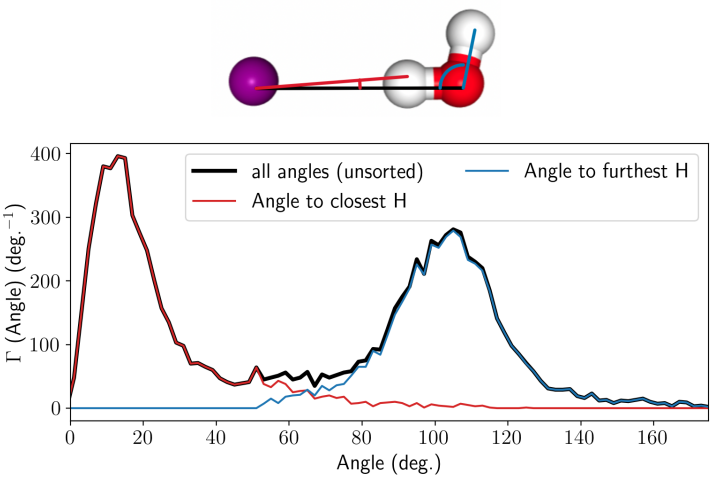

Figure 3: Distribution of the angles between the I atom and the 6 closest waters.

System	Charge (e)	ϵ (kJ / mol)	σ (Å)
I^-	-1	3.69000	5.02000
I^0	0	3.69000	5.02000
I^0_{opt}	0	2.51000	3.75000
O_w	-1.04844	0.68095	3.16435
H_w	0.52422	0	0

Table 3: Non-bonded parameters used in this work. The O_w and H_w parameters are taken from the TIP4PEw force field for water [20], the Lennard-Jones parameters from [21, 22].

TR-XSS data reduction at SACLA

The intensities of the scattered photons $S_{measured}(Q)$ is recorded in a two-dimensional detector. Areas around the central beam stop and between detection panels are masked as seen in Figure 4c). Furthermore, the images are corrected for geometry effects, polarization and absorption of the phosphor layer, which are illustrated in Figure 4a). After azimuthal integration of the corrected 2D images, the amplidude of the scattering signal is scaled to electron units per liquid unit cell (e.u./LUC) for each sample according to its concentration. The scaling factor a is determined by fitting $S_{measured}(Q)$ with a linear combination of a scaled reference for water scattering [23], air scattering and a constant c:

$$S_{fit}(Q) = a \cdot S_{H_2O}(Q) + b \cdot S_{air}(Q) + c \tag{5}$$

The fit as well as water and air scattering contributions are shown in Figure 4d). The inclusion of the constant c indicates that a constant background of the detector is not sufficiently subtracted by the dark subtraction.
Before subtracting the laser-off images from the laser-on images, the scattering curves are filtered for outliers (ΣS deviating from mean(ΣS) by more than 75 %) and normalised in between $Q = 0.75$-5 Å^{-1}. Data sorting with the timing monitor information provided by SACLA is applied to the

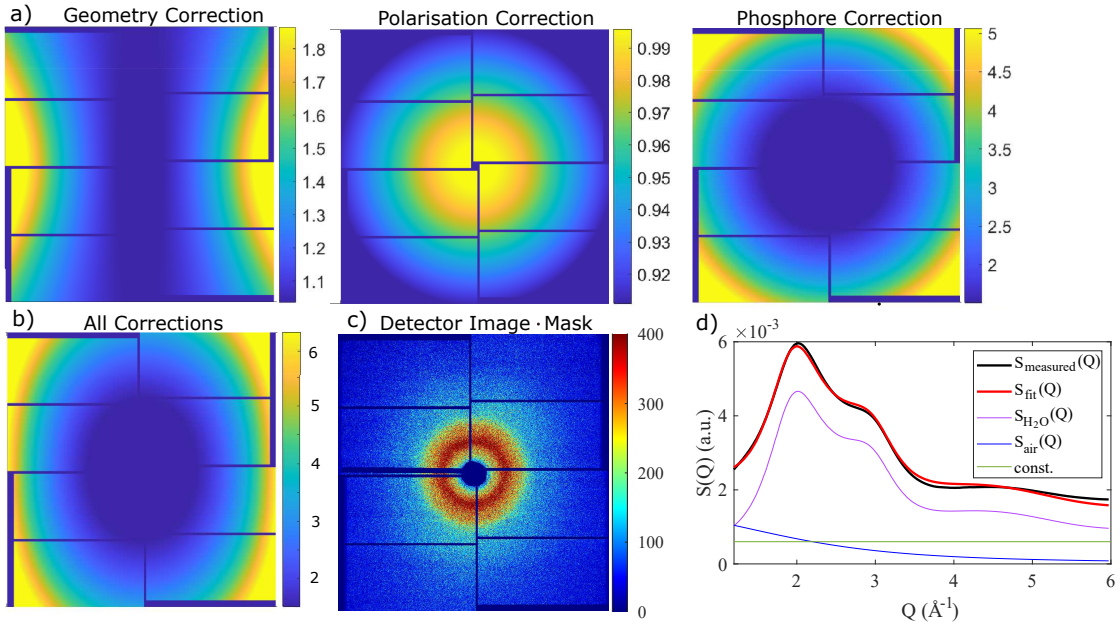

Figure 4: a) Contributions to the detector correction and b) the sum of all detector corrections. c) 2-dim detector image of pure solvent (H_2O) scattering. d) Azimutally integrated scattering curve $S_{measured}(Q)$ (black), fitted with the expected contributions from H_2O scattering, air scattering and an offset.

100 mM NaI dataset, but was not found to influence the analysis results.

Power titration

An onset of coherent multi-photon processes in the excitation of the pump-probe experiments is monitored for both 202 nm and 400 nm laser excitation wavelength. Therefore, the sum of the total intensity $\sum_Q |\Delta S|$ for $Q = 1.5 - 5$ Å^{-1} is plotted as a function of the laser flux in Figure 5. For 202 nm laser excitation, $\sum_Q |\Delta S|$ for aqueous iodide and bromide at 20 mM concentration increases linearly between 2 and 8 μJ laser power. In this linear regime we can assume 1-photon excitation processes for the halides. The difference scattering $\Delta S(Q)$ presented in the main text is collected at 5 μJ, 7 μJ and 8 μJ.

At 400 nm excitation wavelength the laser power titration is performed between $20 - 120\,\mu$J and $\sum_Q |\Delta S|$ increases non-linearly as a function of laser flux. In pure water, no signal ΔS is observed for $< 80\,\mu$J per pulse. Above 80 μJ, we ascribe the grow in of ΔS and the exponential increase of $\sum_Q |\Delta S|$ for water to direct 3-photon excitation of the water molecules and for iodide to a 2-photon excitation process. The scattering ΔS for aqueous iodide at 400 nm as presented in the analysis section B of the SI was taken with 70 μJ and 120 μJ laser flux.

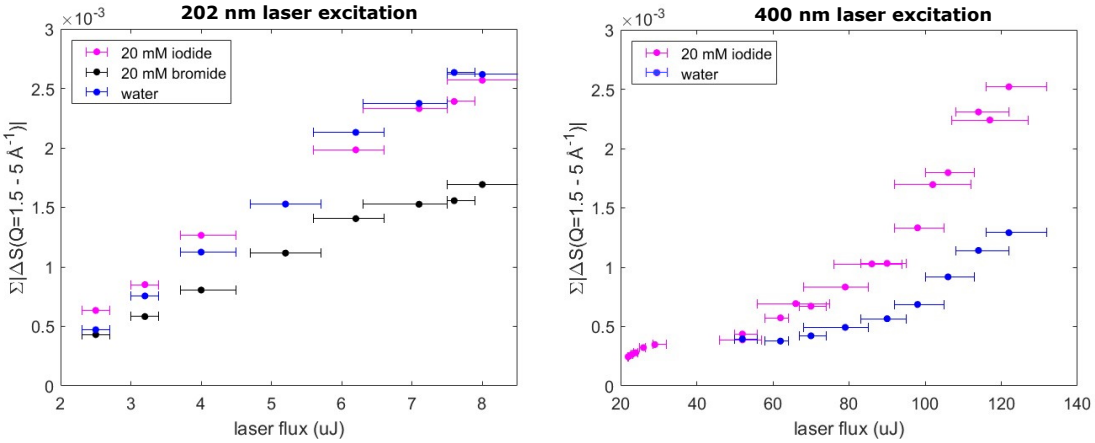

Figure 5: Power titration for 1-photon excitation of the halides at 202 nm and 2-photon excitation of iodide at 400 nm compared to multi-photon excitation of water for both wavelength.

Supplementary Information Part B

Water-subtracted signals

Figure 6-9 show difference scattering as a function of Q and Δt for 20 mM NaI, 100 mM NaBr, 100 mM NaI after 2-photon excitation and 100 mM NaI with long time delays up to $\Delta t = 20$ ps.

$\Delta S(Q, \Delta t)$ is shown scaled to the liquid unit cell. The scaling assumes an unlimited amount of laser photons for the excitation process, which is a good approximation at 20 mM with an optical density (OD) of 1. For higher concentrations the assumption leads to an overestimation of the signal strength, such that after scaling the signal magnitude appears smaller for 100 mM (OD=5) then for the lower concentration data sets.

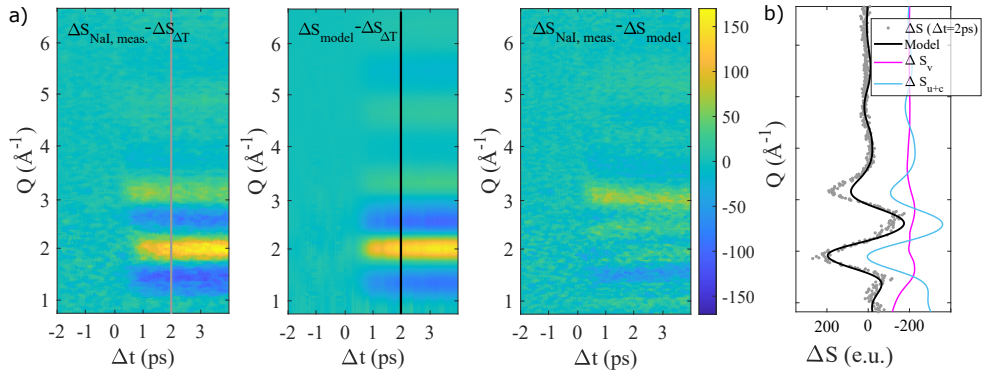

Figure 6: a) The measured signal $\Delta S(Q, \Delta t)$ of 20 mM NaI (water subtracted), the modeled signal and the residual $\Delta S_{measured} - \Delta S_{modeled}$. b) $\Delta S(Q)$ for $\Delta t = 2$ ps.

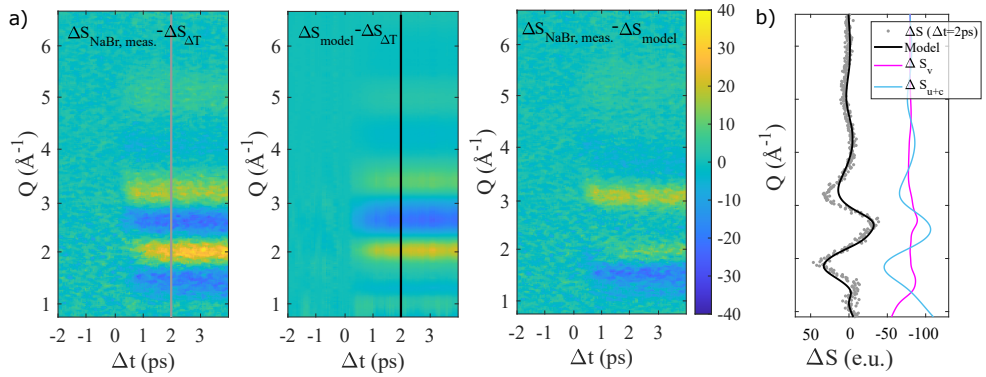

Figure 7: a) The measured signal $\Delta S(Q, \Delta t)$ of 100 mM NaBr (water subtracted), the modeled signal and the residual $\Delta S_{measured} - \Delta S_{modeled}$. b) $\Delta S(Q)$ for $\Delta t = 2$ ps.

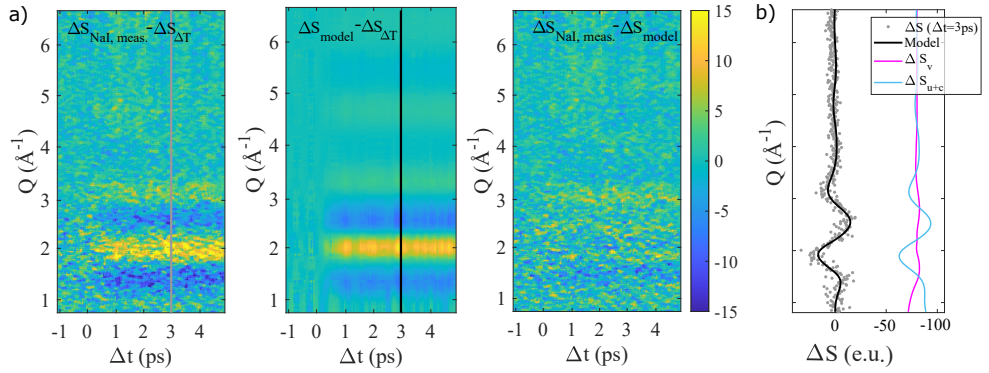

Figure 8: a) The measured signal $\Delta S(Q, \Delta t)$ of 100 mM NaI (water subtracted) after 2-photon excitation, the modeled signal and the residual $\Delta S_{measured} - \Delta S_{modeled}$. b) $\Delta S(Q)$ for $\Delta t = 3$ ps.

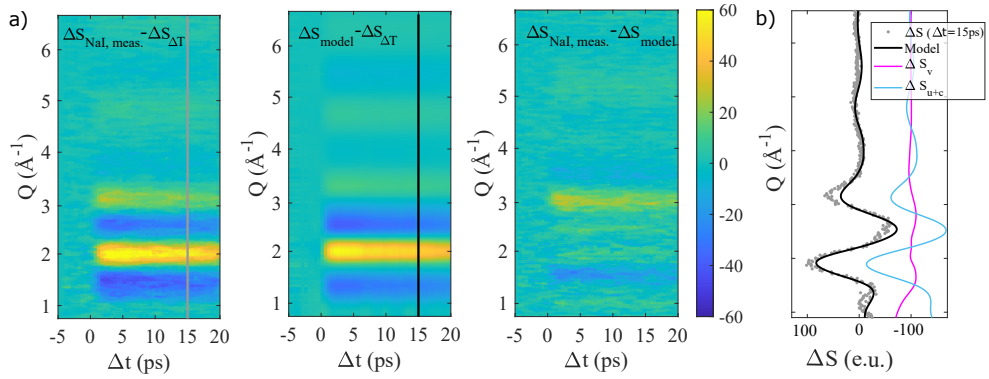

Figure 9: a) The measured signal $\Delta S(Q, \Delta t)$ of 100 mM NaI (water subtracted) for long time delays, the modeled signal and the residual $\Delta S_{measured} - \Delta S_{modeled}$. b) $\Delta S(Q)$ for $\Delta t = 15$ ps.

The density contribution

As described in the main text, our difference scattering data is fitted with

$$\Delta S(Q, \Delta t) = \alpha(\Delta t) \cdot \Delta S_{u+c}(Q) + \gamma(\Delta t) \cdot \Delta S_v(Q) + \Delta T(\Delta t) \cdot \Delta S_{\Delta T}(Q), \tag{6}$$

Beyond this model, additional scattering contributions from significant local heating of the water were seen in previous studies [24]. However, likely due to the much lower laser flux used in this experiment compared to earlier studies, no such heating response could be detected in our signal.

When the solvent scattering $\Delta S_{solv-solv}(Q)$ is calculated from the radial distribution function of O-O, O-H and H-H, the resulting signal seen in Figure 10a (blue line) revels a strong conformity with the density response of the solvent $\Delta S_{\Delta\rho}(Q)$ (green line) [25]. The size of the simulation box is significant for the magnitude of the density like contribution to the signal, as the smaller the box, the larger the density change in the solvent due to the expansion of the cage. For these reasons, we heuristically adjust ΔS_v:

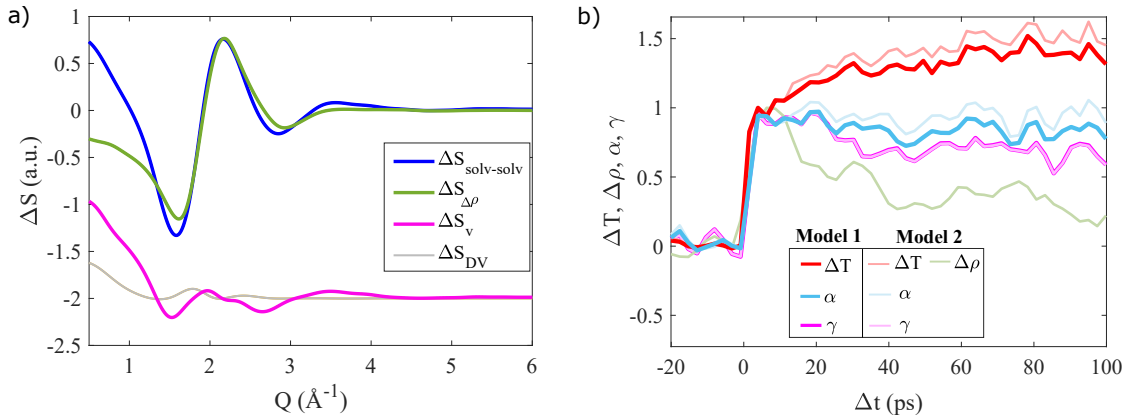

Figure 10: a) Comparison between $\Delta S_{solv-solv}(Q)$ from simulation and the density change contribution $\Delta S_{\Delta\rho}(Q)$. The residual subtracting both curves from each other ($\Delta S_v(Q)$) is plotted together with the displaced volume contribution $\Delta S_{DV}(Q)$. b) Comparison of the the model contributions as a function of delay time Δt in 20 mM aqueous NaBr between Model 1 (used in the main text) and an alternative Model 2 additionally including $\Delta S_{\Delta\rho}(Q)$.

$$\Delta S_v = \Delta S_{solv-solv} - \Delta S_{\Delta\rho} \tag{7}$$

Changes in scattering arising from changes in excluded volume are in the literature [26–28] described by the displaced volume (DV) term. A suggested $\Delta S_{DV}(Q)$ for scattering from a spherical volume is shown in Figure 10a) and has some similarities with $\Delta S_v(Q)$. Alternatively to Model 1, Figure 10b) shows a comparison of the the model contributions as a function of delay time Δt in 20 mM aqueous NaBr between Model 1 and an alternative Model 2 additionally including $\Delta S_{\Delta\rho}(Q)$. The χ^2-value of both models is around $\chi^2 \approx 1.9$. In general, hydrodynamic equilibrium leading to solvent expansion is observed on a nanosecond time scale, which is why the inclusion of $\Delta S_{\Delta\rho}(Q)$ on faster time scales have been put into question as discussed by Kjær et al. [29] However, the potential link between local, transient changes in density and solvated electrons needs to be studied in more detail in the future.

2-photon excitation

The TR-XSS experiment was not only performed with 202 nm but also 400 nm excitation wavelength to study possible effect of 2-photon excitation on the structural dynamics. To investigate the signal dependence on single- or multi-photon excitation on short time scales, Figure 11 shows $U(Q,1)$ and $V(\Delta t,1)$ of ΔS_{NaI} after 1-photon excitation at 202 nm and 2-photon excitation at 400 nm. Both wavelengths excite aqueous iodide into the CTTS band centered at 195 nm. For 2-photon excitation, the lower signal to noise ratio is a consequence of the smaller excitation fraction for the multi-photon process. The shape of $U(Q,1)$ as well as the short time grow-in $V(\Delta t,i)$ show no excitation-dependent changes within the measurement uncertainties. Thus, we conclude that electron-abstraction from a single halide ion in water is a similar process after 1- or 2-photon excitation with the same total energy.

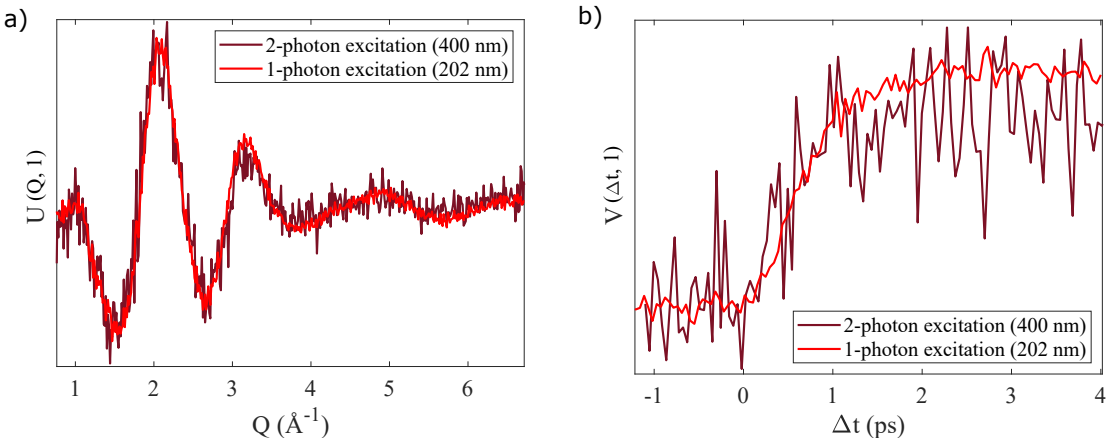

Figure 11: Comparison between 1-photon and 2-photon excitation of the long-lived SVD component observed in all aqueous halide solutions (shown for 100 mM NaI, also see SI). Panel a) depicts $U(Q, 1)$ and in b) the signal grow-in is shown for Δt up to 4 ps.

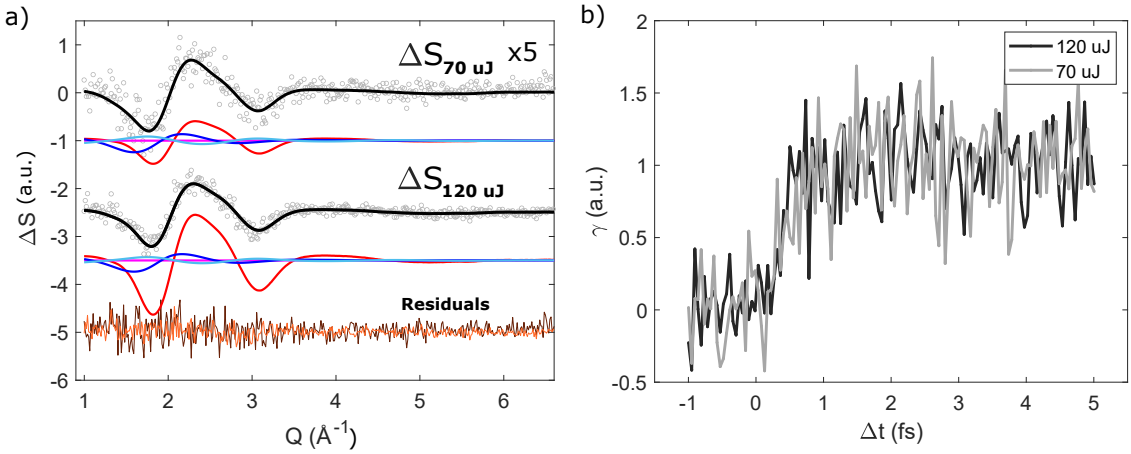

Figure 12: a) Difference signal after 2 ps with 400 nm excitation with 70 μJ and 120 μJ. Shown is 100 mM NaI and signals at 70 μJ were multiplied by 5. The orange line shows the residual at 70 μJ, the brown line at 120 μJ. b) $\gamma(\Delta t)$ as a function of delay time and laser flux.

Furthermore, it was observed that the signal amplitude at 120 μJ after 2-photon excitation of iodide and 3-photon excitation of the water is about five times higher compared to 70 μJ, where no direct solvent excitation occurred (see SI section A, power titration). However, as shown in Figure 12 a), the increase in amplitude results mainly from an increase of the $\Delta S_{\Delta T}$ component (red line). Due to a low excitation yield from the 2-photon excitation process of the iodide, the temporal evolution of other fit components have a low signal-to-noise ratio. An example of $\gamma(\Delta t)$ as a function of delay time and laser flux is shown in Figure 12 b). Here, no significant difference in the structural dynamic could be observed within the noise level.

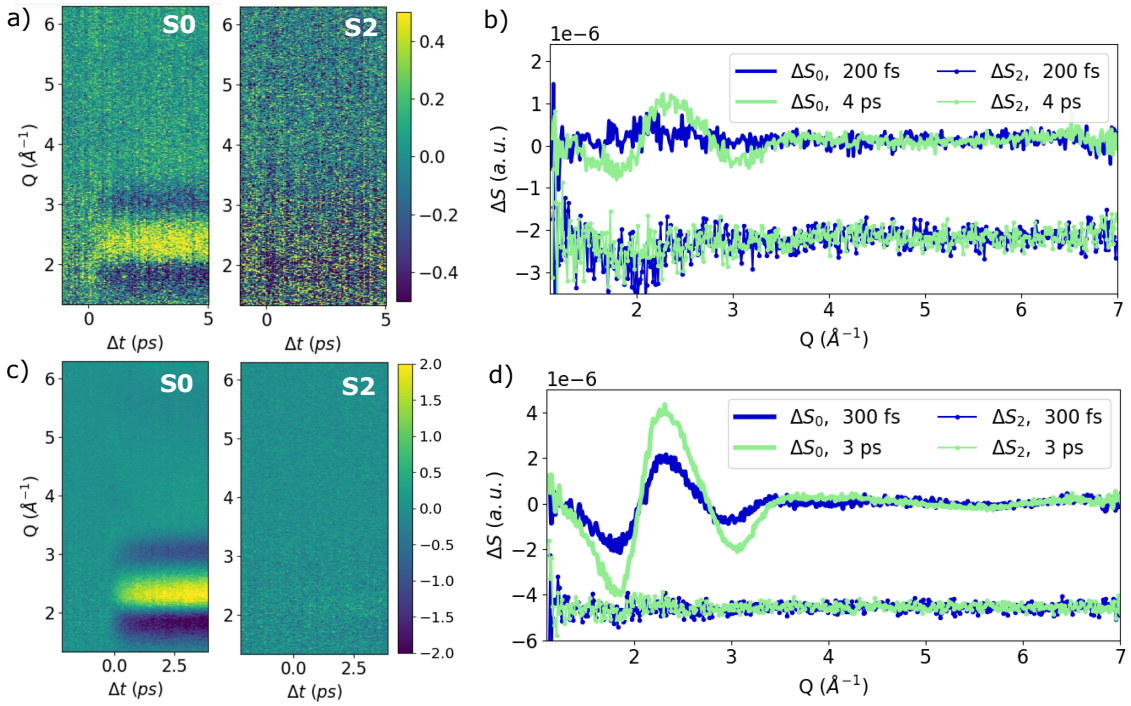

Figure 13: a) S0/S2 decomposition of the 2-photon excited $\Delta S(Q, \Delta t)$ signal of 100 mM NaI. b) Difference signals from a) at two selected time delays. c) S0/S2 decomposition of the 1-photon excited $\Delta S(Q, \Delta t)$ signal of 100 mM NaI, with two time delays shown in d).

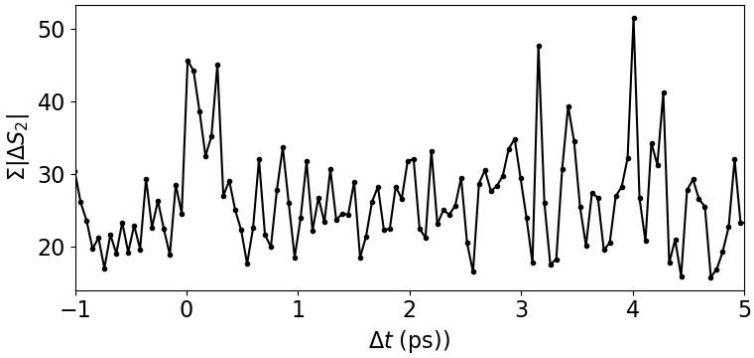

Figure 14: Sum of the absolute values of S2 of 100 mM NaI excited with two photons.

Decomposition of the scattering signal in an isotropic contribution $\Delta S_0(Q, \Delta t)$ and an anisotropic part $\Delta S_2(Q, \Delta t)$ has been shown in previous works [30–32] to contain information about the specific orientation of a molecule with respect to the transition dipole moment. Figure 13 illustrates the decomposition for the difference scattering after 2-photon excitation (top) and after 1-photon excitation (bottom). The time dependent features of the difference scattering signal $\Delta S(Q, \Delta t)$ is in

both cases present in the ΔS_0 contribution but not in the ΔS_2 contribution. However, for 2-photon excitation we find an indication of a minimum in ΔS_2 at $Q = 2$ Å^{-1}. This short lived feature can be explained by a signal contribution form the optical Kerr [33] effect and enables an independent evaluation of time zero in the experiment as shown in Figure 14. Here, the sum of the absolute values was build over range of $Q = 1.4 - 2.6$ Å^{-1} after applying a median filter with a window size of 5 to the Q-axis.

Time-dependence of the scattering signal contributions

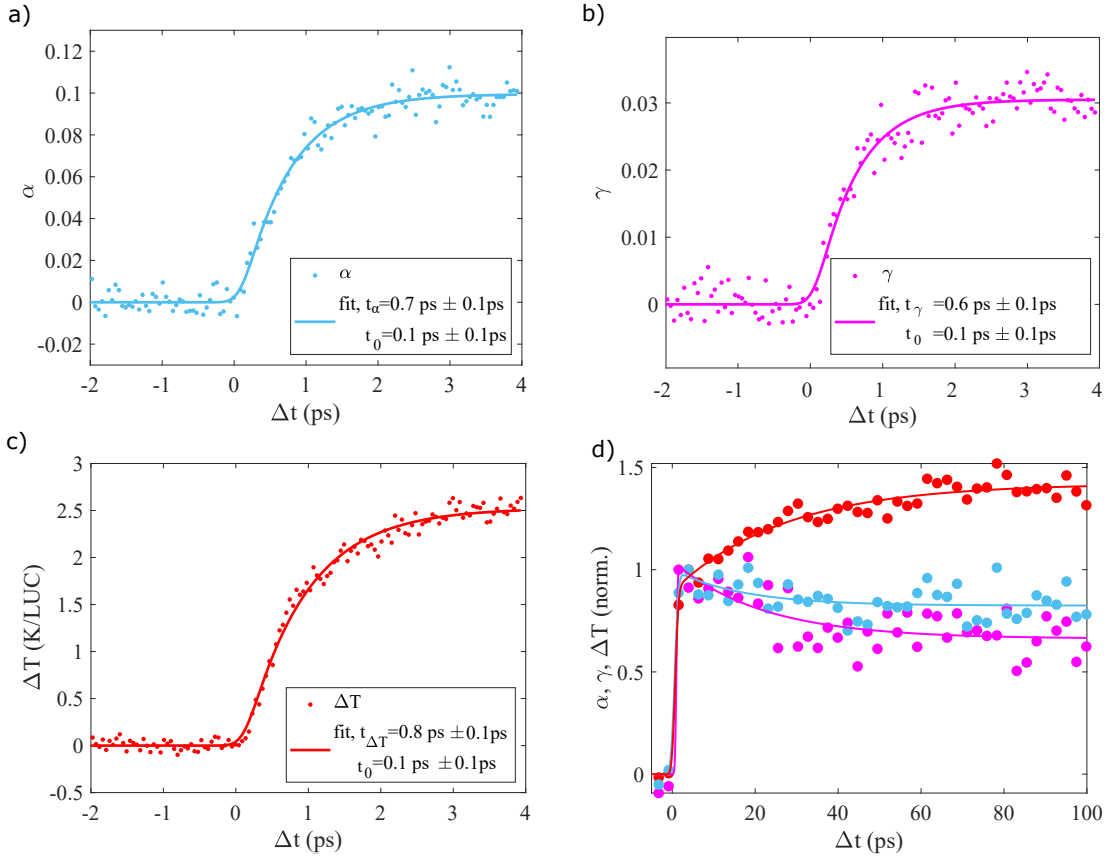

Figure 15: a)-c) Grow-in of the three model contributions $\alpha(\Delta t)$, $\gamma(\Delta t)$ and $\Delta T(\Delta t)$, fitted with Equation 8 for 20 mM aqueous NaBr after excitation with 202 nm. d) Comparison between the long time delay behaviour of $\alpha(\Delta t)$, $\gamma(\Delta t)$ and $\Delta T(\Delta t)$. The solid lines are a fitted broadened exponential decay (characteristic times $\tau_{\alpha 2}$, $\tau_{\gamma 2}$) with an offset$>$ 50% of the signal magnitude. A double exponential function was fitted to ΔT (characteristic time $\tau_{\Delta T 2}$).

Figure 15 shows the the characteristic times τ fitted to a set of difference scattering data from 20 mM aqueous NaBr after excitation with 202 nm. Rise times τ_α, τ_γ and $\tau_{\Delta T}$ are similar to the results presented for aqueous NaI in the main text, where an exponential increase f is described by a convolution with a Gaussian shaped instrument response function g:

$$(g * f)(x) = \frac{1}{2}h\Big(1 - exp(\frac{(2t_0\tau + \sigma^2)}{(2\tau^2)})exp(\frac{-x}{\tau}) \\ +erf(\frac{t_0\tau - \tau x + \sigma^2}{\sigma\tau\sqrt{2}})exp(\frac{2t_0\tau + \sigma^2}{2\tau^2})exp(\frac{-x}{\tau}) - erf(\frac{t_0 - x}{\sigma\sqrt{2}})\Big). \tag{8}$$

For long delay times up to $\Delta t = 100\,\text{ps}$ as shown in Figure 15d, the fitted decay times $\tau_{\alpha 2}$, $\tau_{\gamma 2}$ and the second, slower rise time $\tau_{\Delta T 2}$ also follow the trends observed for aqueous NaI. The following heuristic fitting model was used for the decay of $\tau_{\alpha 2}$ and $\tau_{\gamma 2}$ after smoothing the data, using a moving average filter with span 3:

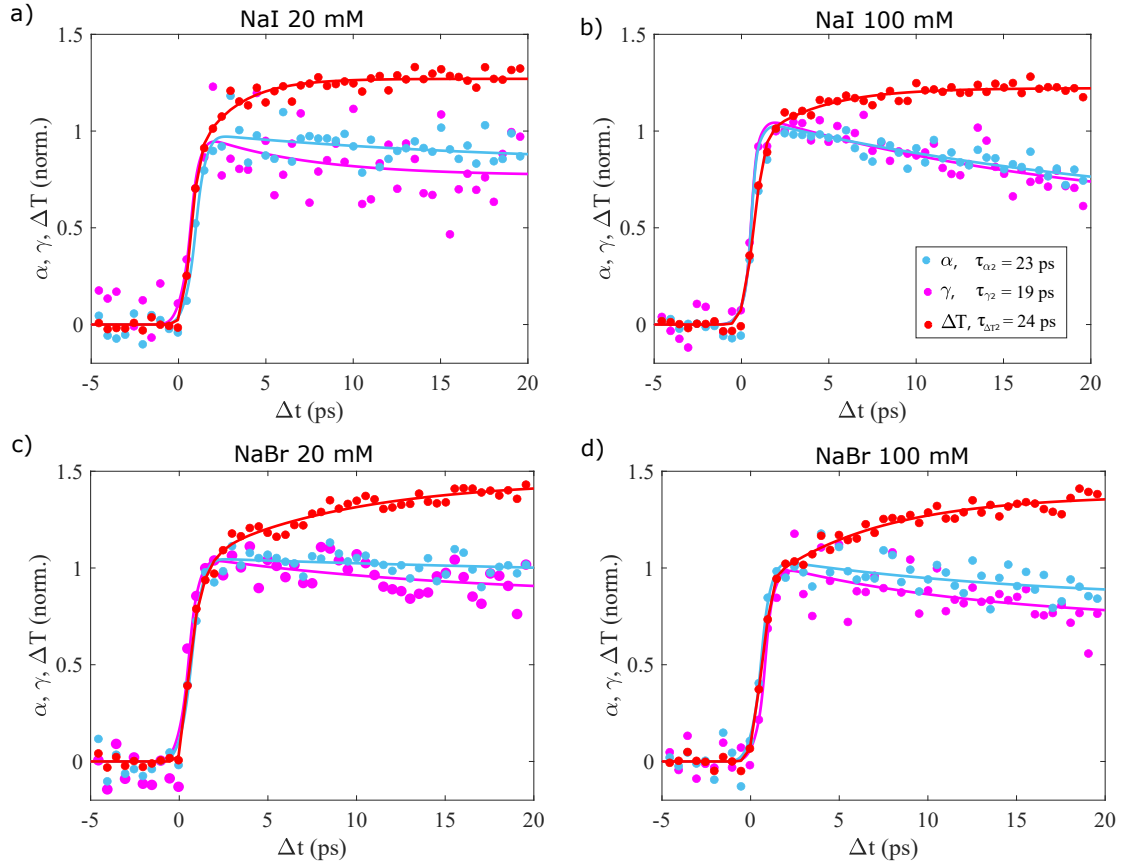

Figure 16: Comparison of the behaviour of $\alpha(\Delta t)$, $\gamma(\Delta t)$ and $\Delta T(\Delta t)$ up to $\Delta t = 20\,\text{ps}$ for NaI and NaBr at different concentrations.

$$h \cdot \left(0.5 \cdot \exp(\frac{\sigma^2 - 2 \cdot (x - t_0) \cdot \tau}{2 \cdot \tau^2}) \cdot (1 - \operatorname{erf}(\frac{\sigma - (x - t_0) \cdot \tau}{\sqrt{2} \cdot \sigma \cdot \tau})) \right. \\ \left. + \frac{1}{2} \cdot \left(1 - \operatorname{erf}(\frac{\sigma^2 - (x - t_0) \cdot \tau_2}{\sqrt{2} \cdot \sigma \cdot \tau_2})\right) \cdot p. \right. \tag{9}$$

Here, h indicates the height of the the increase, t_0 is the midway point of the Gaussian providing information on when the exponential growth begins, σ is the standard deviation, τ are the lifetimes of the decay and p is a constant describing the height of the plateau, which was fixed in for each fit to a value approximated at Δt =20 ps. Furthermore, the second lifetime τ_2 in Equation 9 ascribed to geminate recombination was fixed to the value of 120 ps in accordance with τ_3 measured with TAS.

For the rise of $\tau_{\Delta T2}$, a double exponential increase has been convoluted with a Gaussian similar to Equation 8:

$$\begin{aligned} &\frac{h}{2}[(1+erf(\frac{x-t_0}{\sqrt{2}\sigma}))-e^{\frac{\sigma^2-2(x-t_0)\tau}{2\tau^2}}\cdot(1-erf(\frac{\sigma^2-(x-t_0)\tau}{\sqrt{2}\sigma\tau}))] \\ +&\frac{h_2}{2}[(1+erf(\frac{x-t_0}{\sqrt{2}\sigma}))-e^{\frac{\sigma^2-2(x-t_0)\tau_2}{2\tau_2^2}}\cdot(1-erf(\frac{\sigma^2-(x-t_0)\tau_2}{\sqrt{2}\sigma\tau_2}))]. \end{aligned} \tag{10}$$

Electron Ejection Radius

The distance between an halide and an ejected electron was estimated from the decay of $\alpha(\Delta t)$ (Figure 17a) for NaI and NaBr as described by Vester et al. [24] in the diffusion limited model. The resulting distributions of the electron ejection radii r_{ej} are shown in Figure 17b and the fits are can be seen in c) for NaI and d) for NaBr.

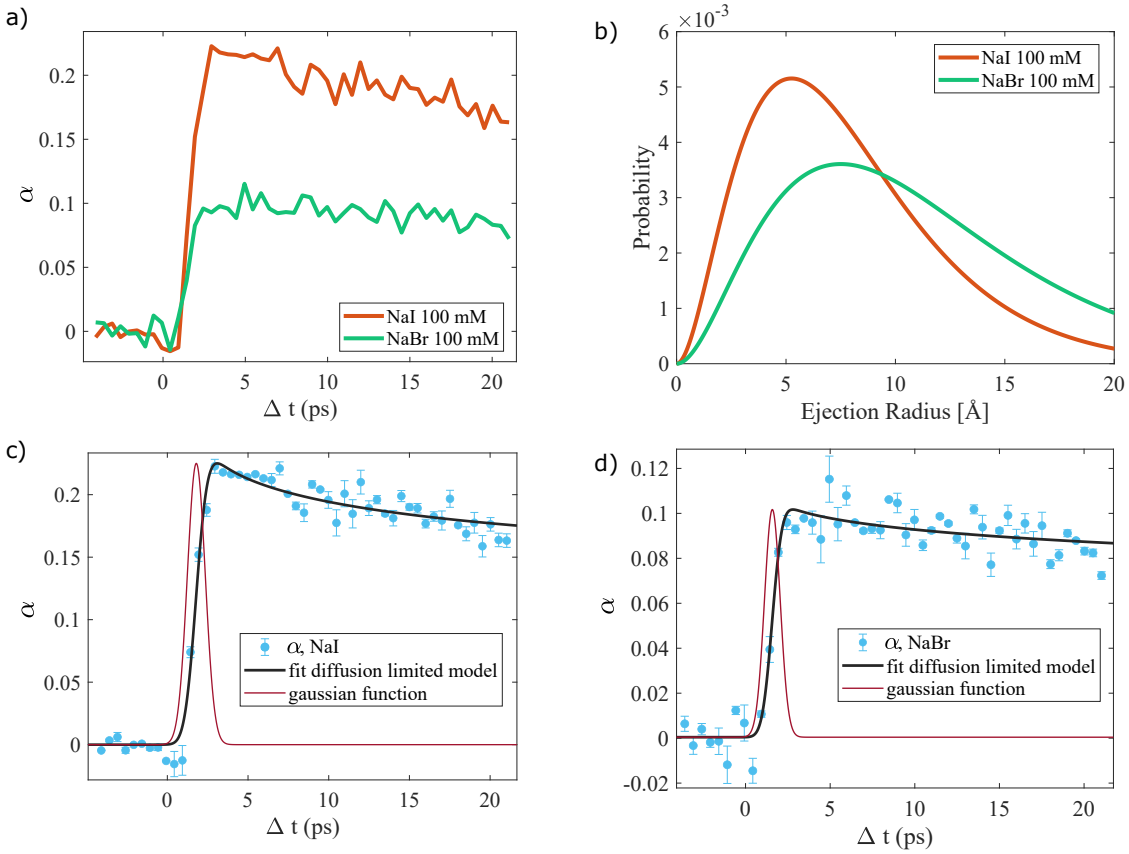

Figure 17: a) Decay of $\alpha(\Delta t)$ for iodide and bromide and b) the estimated electron ejection radius. c) and d) Fit of the diffusion limited model to NaI and NaBr.

ESRF data analysis

Diiodide and triiodide

In the data measured at ESRF, the photo-products

$$\begin{aligned} I^- + I &\rightarrow I_2^- \\ I_2^- + I &\rightarrow I_3^- \end{aligned}$$

were taken into account for modeling $\Delta S(Q, \Delta t)$. Thus, for the picosecond-resolved data (synchrotron data), Equation 6 is modified to

$$\begin{aligned} \Delta S(Q, \Delta t) = \alpha(\Delta t) \cdot \Delta S_{u+c}(Q) + \Delta T(\Delta t) \cdot \Delta S_{\Delta T}(Q) \\ + \eta(\Delta t) \cdot \Delta S_{I_2}(Q) + \xi(\Delta t) \cdot \Delta S_{I_3}(Q). \end{aligned} \tag{11}$$

Contributions to the difference scattering $\Delta S(Q, \Delta t = 200ps)$ are shown in Figure 18.

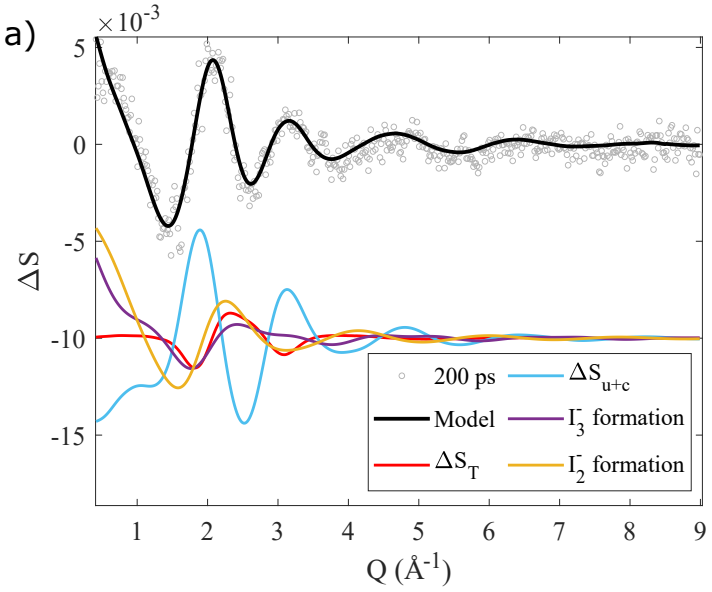

Figure 18: ΔS measured at ESRF fitted with Equation 11. Shown are the fit and fit contributions.

Lennard-Jones potentials

As described in the main text, the choice of the Lennard-Jones potential influences ΔS_{u+c}. Figure 20 demonstrates the fit of the model in Equation 6 to the measured data $\Delta S_{NaI}(Q, \Delta t) - \Delta S_{H_2O}(Q, \Delta t > 2.6\,ps)$ after 1-photon excitation for the two sets of Lennard-Jones parameters. If a potential I^0_{opt} is assumed for ΔS_{u+c} ($\sigma = 3.75$ Å^{-1}, $\epsilon = 2.51\,\frac{\text{kJ}}{\text{mol}}$), the residual $\Delta S_{measured} - \Delta S_{modeled}$ is lowered compared to an assumed I^0 ($\sigma = 5.02$ Å^{-1}, $\epsilon = 3.69\,\frac{\text{kJ}}{\text{mol}}$).

Scattering from water after excitation with 202 nm laser pulses

The scattering contribution $\Delta S_{\Delta T}$ from literature [25] is in good accordance with the measured difference scattering observed from water at $\Delta t = 2$ ps after excitation with a 202 nm laser pulse (see Figure 20). The solvent (heat) response of the three main data sets on neat water and 100 mM of NaI and NaBr is compared in Figure21. The magnitudes of the contributions differ and the kinetics may hold interesting information on the energetics involved in electron-abstraction and subsequent localization processes. However, scaling to the liquid unit cell assumes homogeneous excitation throughout the liquid jet, which at the studied concentrations resulting in an optical density up to 5 could not be uphold. Thus, quantitative determination of pure water scattering amplitudes is difficult.

Regarding the ΔT parameter in Equation (3) of the main manuscript, we note that temperature is an equilibrium property of a thermodynamic system and therefore strictly not defined on these ultrafast time scales after a photo-excitation event. However, as discussed in detail in the SI of reference [14] of the main manuscript, ΔT in the present context arises as a measure of the intramolecular structural change in the solvent due to a deposition of energy. As this measure is linear as a function of the temperature change measured on equilibrium time scales, $\Delta S_{ChangeDueToHeat} =$

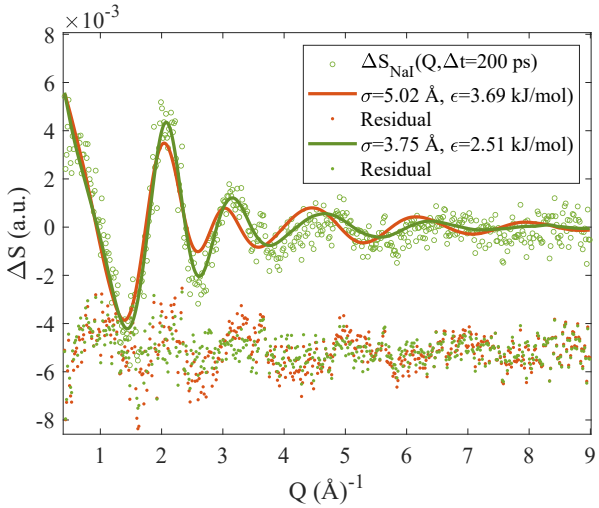

Figure 19: Comparison of the fits using two different sets of Lennard-Jones parameters in the modelling of $\Delta S_{NaI}(Q, \Delta t) - \Delta S_{H_2O}(Q, \Delta t > 2.6\, ps)$.

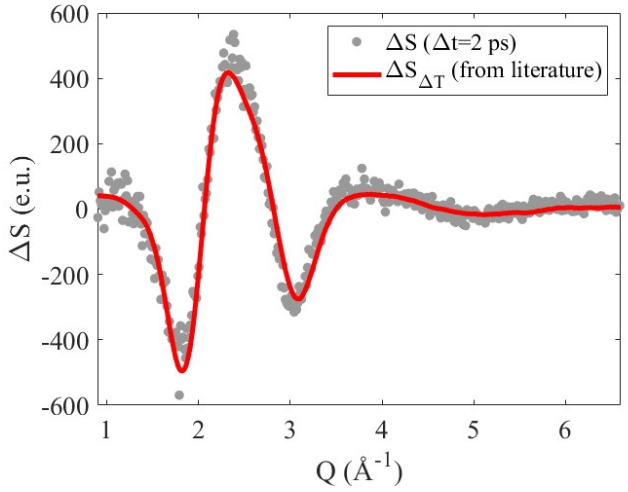

Figure 20: Scattering signal $\Delta S(Q, \Delta t = 2ps)$ from water after excitation with 202 nm laser pulses.

$\Delta T \cdot \Delta S_{\Delta T}$ this measure can be related to a temperature after thermodynamic equilibrium has been established, as long as the local perturbation of solvent structure due to energy deposition is within the linear regime, which is on the order of tens of K. We further note that inclusion of a second-order temperature term as in reference [34] to account for local "heating" exceeding the linearity regime did not lead to a significantly better fit.

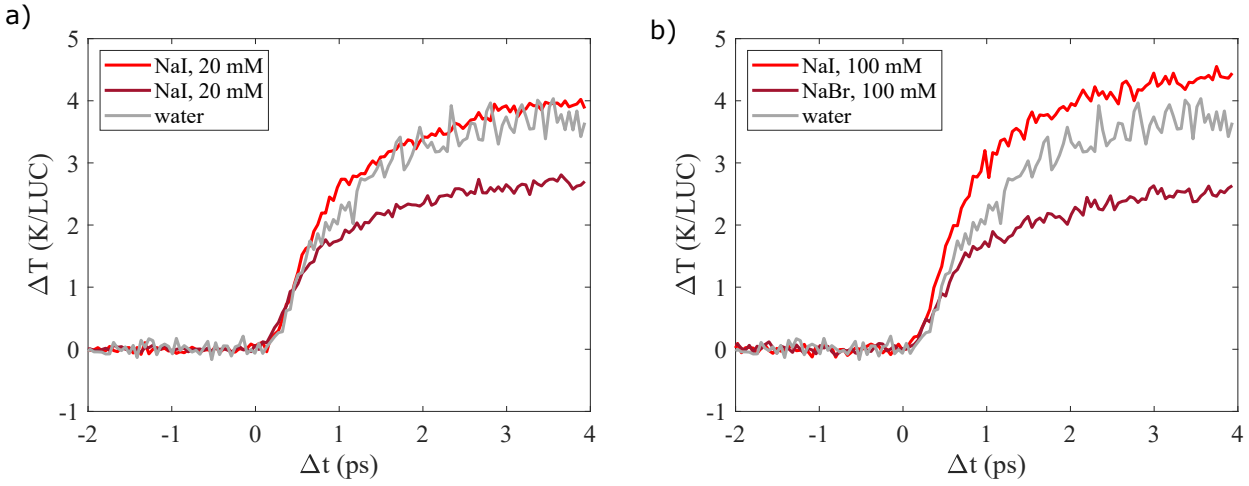

Figure 21: The fitted scattering contribution $\Delta T(\Delta t)$ for aqueous NaI, NaBr and pure water.

References

[1] F Renth et al. "Ultrafast transient absorption spectroscopy of the photo-induced Z–E isomerization of a photochromic furylfulgide". In: *Chemical physics letters* 428.1-3 (2006), pp. 62–67.

[2] K Röttger et al. "A femtosecond pump–probe spectrometer for dynamics in transmissive polymer films". In: *Applied Physics B* 118 (2015), pp. 185–193.

[3] Ron Siewertsen et al. "Parallel ultrafast E–C ring closure and E–Z isomerisation in a photochromic furylfulgide studied by femtosecond time-resolved spectroscopy". In: *Physical Chemistry Chemical Physics* 11.28 (2009), pp. 5952–5961.

[4] Uta C Stange and Friedrich Temps. "Ultrafast electronic deactivation of UV-excited adenine and its ribo-and deoxyribonucleosides and-nucleotides: A comparative study". In: *Chemical Physics* 515 (2018), pp. 441–451.

[5] Hans P Good, Alan J Kallir, and Urs P Wild. "Comparison of fluorescent lifetime fitting techniques". In: *The Journal of Physical Chemistry* 88.22 (1984), pp. 5435–5441.

[6] Peter Eastman et al. "OpenMM 7: Rapid development of high performance algorithms for molecular dynamics". In: *PLOS Computational Biology* 13.7 (July 2017). Ed. by Robert Gentleman, e1005659. DOI: 10.1371/journal.pcbi.1005659. URL: https://doi.org/10.1371/journal.pcbi.1005659.

[7] D.A. Case et al. *Amber 2021*. 2021.

[8] Jesús A Izaguirre, Christopher R Sweet, and Vijay S Pande. "Multiscale dynamics of macromolecules using normal mode Langevin". In: *Biocomputing 2010*. World Scientific, 2010, pp. 240–251.

[9] Asmus O Dohn et al. "On the calculation of x-ray scattering signals from pairwise radial distribution functions". In: *Journal of Physics B: Atomic, Molecular and Optical Physics* 48.24 (2015), p. 244010.

[10] Debdas Dhabal et al. "Probing the triplet correlation function in liquid water by experiments and molecular simulations". In: *Physical Chemistry Chemical Physics* 19.4 (2017), pp. 3265–3278. DOI: 10.1039/c6cp07599a. URL: https://doi.org/10.1039/c6cp07599a.

[11] AO Dohn et al. "Eliminating finite-size effects on the calculation of x-ray scattering from molecular dynamics simulations". In: *The Journal of Chemical Physics* 159.12 (2023).

[12] L. Martínez et al. "PACKMOL: A package for building initial configurations for molecular dynamics simulations". In: *Journal of Computational Chemistry* 30.13 (Oct. 2009), pp. 2157–2164. DOI: 10.1002/jcc.21224. URL: https://doi.org/10.1002/jcc.21224.

[13] Kyung Hwan Kim et al. "Solvent-dependent molecular structure of ionic species directly measured by ultrafast x-ray solution scattering". In: *Physical review letters* 110.16 (2013), p. 165505.

[14] Ilan Benjamin and Robert M Whitnell. "Vibrational relaxation of I- 2 in water and Ethanol: Molecular dynamics simulation". In: *Chemical physics letters* 204.1-2 (1993), pp. 45–52.

[15] Benjamin G Levine, John E Stone, and Axel Kohlmeyer. "Fast analysis of molecular dynamics trajectories with graphics processing units—Radial distribution function histogramming". In: *Journal of computational physics* 230.9 (2011), pp. 3556–3569.

[16] Pritam Ganguly and Nico FA van der Vegt. "Convergence of sampling Kirkwood–Buff integrals of aqueous solutions with molecular dynamics simulations". In: *Journal of chemical theory and computation* 9.3 (2013), pp. 1347–1355.

[17] E Lorch. "Neutron diffraction by germania, silica and radiation-damaged silica glasses". In: *Journal of Physics C: Solid State Physics* 2.2 (1969), p. 229.

[18] H. A. Lorentz. "Ueber die Anwendung des Satzes vom Virial in der kinetischen Theorie der Gase". In: *Annalen der Physik* 248.1 (1881), pp. 127–136. DOI: 10.1002/andp.18812480110. URL: https://doi.org/10.1002/andp.18812480110.

[19] Daniel Berthelot. "Sur le mélange des gaz". In: *Comptes rendus hebdomadaires des séances de l'Académie des Sciences* 126 (1898), pp. 1703–1855.

[20] Hans W. Horn et al. "Development of an improved four-site water model for biomolecular simulations: TIP4P-Ew". In: *The Journal of Chemical Physics* 120.20 (2004), pp. 9665–9678. DOI: 10.1063/1.1683075. URL: https://doi.org/10.1063/1.1683075.

[21] William L Jorgensen, Jakob P Ulmschneider, and Julian Tirado-Rives. "Free energies of hydration from a generalized Born model and an ALL-atom force field". In: *The Journal of Physical Chemistry B* 108.41 (2004), pp. 16264–16270.

[22] Pengfei Li, Lin Frank Song, and Kenneth M Merz Jr. "Systematic parameterization of monovalent ions employing the nonbonded model". In: *Journal of chemical theory and computation* 11.4 (2015), pp. 1645–1657.

[23] Katrin Amann-Winkel et al. "X-ray and neutron scattering of water". In: *Chemical reviews* 116.13 (2016), pp. 7570–7589.

[24] Peter Vester et al. "Tracking structural solvent reorganization and recombination dynamics following e- photoabstraction from aqueous I- with femtosecond x-ray spectroscopy and scattering". In: *The Journal of Chemical Physics* 157.22 (2022), p. 224201.

[25] Kasper Skov Kjær et al. "Introducing a standard method for experimental determination of the solvent response in laser pump, X-ray probe time-resolved wide-angle X-ray scattering experiments on systems in solution". In: *Physical Chemistry Chemical Physics* 15.36 (2013), pp. 15003–15016.

[26] RDB Fraser, TP MacRae, and E Suzuki. "An improved method for calculating the contribution of solvent to the X-ray diffraction pattern of biological molecules". In: *Journal of Applied Crystallography* 11.6 (1978), pp. 693–694.

[27] Po-chia Chen and Jochen S Hub. "Validating solution ensembles from molecular dynamics simulation by wide-angle X-ray scattering data". In: *Biophysical journal* 107.2 (2014), pp. 435–447.

[28] Jochen S Hub. "Interpreting solution X-ray scattering data using molecular simulations". In: *Current opinion in structural biology* 49 (2018), pp. 18–26.

[29] Kasper S Kjær et al. "Finding intersections between electronic excited state potential energy surfaces with simultaneous ultrafast X-ray scattering and spectroscopy". In: *Chemical science* 10 (2019), pp. 5749–5760. DOI: https://doi.org/10.1039/c8sc04023k.

[30] Kristoffer Haldrup et al. "Ultrafast X-ray scattering measurements of coherent structural dynamics on the ground-state potential energy surface of a diplatinum molecule". In: *Physical review letters* 122.6 (2019), p. 063001.

[31] Andrés Montoya-Castillo et al. “Optically Induced Anisotropy in Time-Resolved Scattering: Imaging Molecular-Scale Structure and Dynamics in Disordered Media with Experiment and Theory”. In: *Physical Review Letters* 129.5 (2022), p. 056001.

[32] Ulf Lorenz, Klaus Braagaard Møller, and Niels Engholm Henriksen. “On the interpretation of time-resolved anisotropic diffraction patterns”. In: *New Journal of Physics* 12.11 (2010), p. 113022.

[33] Hosung Ki et al. “Optical Kerr effect of liquid acetonitrile probed by femtosecond time-resolved x-ray liquidography”. In: *Journal of the American Chemical Society* 143.35 (2021), pp. 14261–14273.

[34] Kristoffer Haldrup et al. “Observing solvation dynamics with simultaneous femtosecond X-ray emission spectroscopy and X-ray scattering”. In: *The journal of physical chemistry B* 120.6 (2016), pp. 1158–1168.